Defect formation and diffusion mechanism in ion-assisted molecular-beam epitaxy

C. J. Tsai,* T. Vreeland, Jr., and H. A. Atwater

Thomas J. Watson Laboratory of Applied Physics, California Institute of Technology, Pasadena, California 91125

A simple moving boundary diffusion model has been used to characterize defect incorporation kinetics during ion-assisted molecular-beam epitaxy. The model permits analysis of the dependence of the final defect concentration on the growth rate, defect diffusivity, defect production range, and the shape of defect depth distribution. The results indicate a linear dependence of the final defect concentration on the ion-to-atom flux ratio which is in the growth-rate-limited regime of the model. Comparison between the model and the film strains measured by x-ray rocking curve analyses has been made and reveals that the thermal spike energy deposited by the bombarding ions during epitaxial growth has a significant effect on the apparent activation energy of the defect migration. A transition temperature above which the defect migration is thermally activated and below which the defect migration is cascade assisted can be defined. The experimentally observed temperature dependence of the defect concentration can be attributed to cascade-assisted diffusion of the defects. Comparison between the model and the multisite multiply activated migration model for low-energy dopant incorporation has also been made. The results show the similarity between the defect incorporation and dopant incorporation which gives a unified view of both processes.

I. INTRODUCTION

Low-energy ion beams have been used as an extra control element for semiconductor processing. The applications include sputtering, surface cleaning, enhanced dopant incorporation,[1] surface smoothing,[2-5] growth mode modification,[6] and strain modification.[7,8] Direct low-energy ion-beam deposition,[9] partially-ionized vapor deposition,[10] ion-beam sputter deposition,[11,12] and concurrent low-energy ion bombardment during sputtering deposition[13] also produced Si homoepitaxial films at much lower growth temperature compared to the conventional thermal molecular-beam epitaxy (MBE).

During low-energy ion bombardment, injection of pointlike defects into the subsurface region results in entrapment of defects. When low-energy ion bombardment is combined with epitaxial growth at a constant rate, the resulting uniform dispersion of pointlike defects leads to uniformly strained epitaxial layers. The linear dependence of the strain on the ion-to-atom flux ratio[7,8] suggests that defect recombination is consistent with first-order kinetics and that the major sink for defect annihilation is the free surface. Following these assumptions, we can conceptualize the steady-state defect concentration as a simple moving boundary diffusion problem using a continuum approximation. The activation processes for defect diffusion were explained via a cascade-assisted diffusion model which is activated by the thermal spike energy deposited by the bombarding ions. A multisite multiply activated migration model of low-energy ion-beam-enhanced dopant incorporation using surface, bulk, and three intermediate sites with different activation barriers has been proposed by Ni et al.[14] A qualitative comparison of the present work with this model was also discussed.

II. EXPERIMENT

Experiments were done in a custom-designed molecular-beam epitaxy system with a base pressure of 1×10^{-10} Torr. The system is equipped with two electron guns for deposition of Si and Ge, a Kaufmann-type ion source capable of producing ions at energies of 50–1500 eV, and a reflection high-energy electron-diffraction (RHEED) apparatus. Strain-modified films of 100 nm were grown at rates which ranged from 0.1 to 0.7 nm/s on (001) Ge substrates with concurrent ion-beam bombardment. The growth conditions including ion species, growth rate, and ion flux are listed in Table I. RHEED was used for *in situ* monitoring of the surface. A four-crystal high-resolution x-ray diffractometer[15] using a Cu-$K_{\alpha 1}$ radiation source was employed to analyze the film strains. Comparison of experimental data with simula-

TABLE I. Growth conditions of IAMBE Ge films on Ge(001) substrate with concurrent 200-eV Ar^+ ion beams and 200-eV Xe^+ ion beams at 300 °C.

Growth rate (nm/s)	Ion flux $\mu A/cm^2$	Ions/atoms	Strain (%)	Ions
0.60	4.20	0.010	0.20	Ar^+
0.30	4.68	0.022	0.53	Ar^+
0.35	6.45	0.026	0.95	Ar^+
0.25	6.13	0.035	0.82	Ar^+
0.24	7.58	0.045	1.57	Ar^+
0.30	4.84	0.023	0.17	Xe^+
0.20	5.97	0.042	0.44	Xe^+
0.17	8.06	0.067	0.29	Xe^+
0.10	9.68	0.137	0.61	Xe^+

tions based on dynamical x-ray-diffraction theory[16] was used to determine the strains.

III. RESULTS AND DISCUSSIONS

A. IAMBE Growth

1. Moving boundary diffusion model

We consider the growth surface to be a one-dimensional system in a frame moving with velocity v, by substituting $x + vt$ for x into the diffusion equation and assuming the diffusivity of the defects at the growth temperature D is independent of concentration. We have

$$\frac{dN}{dt} = D\frac{d^2N}{dx^2} - v\frac{dN}{dx} + S , \qquad (1)$$

where N is the defect concentration, x is the distance measured from the moving growth surface, v is the growth rate, and S is the source function representing the defect profile generated by the ion beam. We are interested in the steady-state solution, $dN/dt = 0$. Equation (1) is basically the same as the diffusion equation used by Myers-Beaghton[17] for studying the diffusion and adatom interaction during epitaxial growth on a vicinal surface without a recombination term. We choose two simple source functions, (i) a step function and (ii) a Gaussian function, as shown in Fig. 1. The choice of the step function is to illustrate the functional dependence of the important parameters in the ion-assisted molecular-beam epitaxy (IAMBE) process. We define a projected defect production range R_p for the step source function, above which the defect production rate can be ignored. In the Gaussian source function, ΔR_p is the standard deviation of the projected defect production range. The quantities R_p and ΔR_p have the usual meaning when we deal with
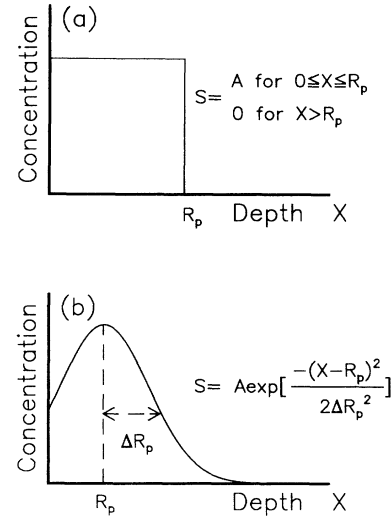

FIG. 1. Defect production profiles used for analytic solution of Eq. (1) with total defects per uit area per unit time. (a) A step function with defect production range R_p, (b) a Gaussian with defect production range R_p and standard range deviation ΔR_p.

the dopant incorporation, i.e., R_p is the projected range and ΔR_p is the range straggling. We also define $\alpha = v/D$. For purposes of comparison of these two source functions, we fixed the total defect flux (per unit surface area per unit time) and set it equal to K. The boundary conditions used in solving the problem for the step function are $N(0) = 0, N(\infty) = C$; N is continuous at position R_p, and the slope of N at position R_p is also continuous and for the Gaussian function they are $N(0) = 0, N(\infty) = C$, and the slope of N at $x = \infty$ is 0. The solutions for the final concentration in these two cases are the following:

$$\text{(i)} \quad C = \frac{K}{v} + \frac{K}{\alpha R_p v}(e^{-\alpha R_p} - 1) ,$$

$$\text{(ii)} \quad C = \frac{K}{v}\left\{1 - \frac{e^{-\alpha R_p + \alpha^2 \Delta R_p^2/2}\,\text{erfc}\left[-\frac{R_p}{\sqrt{2}\Delta R_p} + \frac{\alpha \Delta R_p}{\sqrt{2}}\right]}{\left[1 + \text{erf}\left[\frac{R_p}{\sqrt{2}\Delta R_p}\right]\right]}\right\} . \qquad (2)$$

For the step defect distribution, the final defect concentrations in the growth-rate-limited regime, $\alpha R_p \gg 1$, are proportional to K/v, while in the diffusion-limited regime, $\alpha R_p \ll 1$, the final concentrations are proportional to KR_p/D. For the Gaussian defect distribution, the final concentration C can be proved to be convergent and the criterion for achieving the growth-rate-limited regime depends on the value of $M = R_p/\sqrt{2}\Delta R_p$. The sufficient condition for the growth-rate-limited regime is $\alpha R_p \gg 2M + M^2$, while for $M \gg 1$, the exponential term in Eq. (2ii) will dominate the approach of the final concentration to K/v, the condition becomes $\alpha R_p \gg 1$. The

condition states that, for a fixed defect production range, broader defect production profiles require higher growth rates to trap all the defects. Note that K is proportional to the ion flux, J_i. Figure 2 shows the final concentrations as a function of αR_p for the step function and the Gaussian functions with $M = 0.707$ and 2.828. The final defect concentration of a step source function never reaches unity because a certain portion of the defects can be classified as surface defects. This clearly shows that, in the IAMBE processes, the definition of surface defects (defects that are generated in the substrate and escape out of the substrate), and bulk defects (defects that are gen-
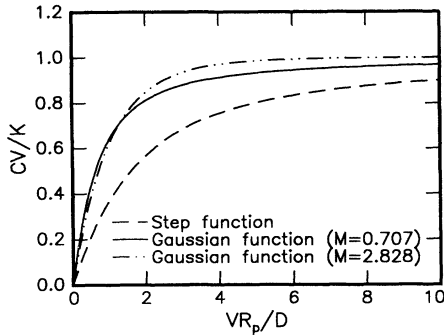
FIG. 2. The dependence of the final normalized defect concentrations on αR_p for a step source function, a Gaussian source function with $R_p/\sqrt{2}\Delta R_p = 0.707$, and a Gaussian source function with $R_p/\sqrt{2}\Delta R_p = 2.828$.

erated and trapped in the substrate), are not only related to the diffusivity of defects and the defect production profile but also to the growth velocity. Let us use the step-function case to illustrate the definition of the surface defects and bulk defects in the IAMBE process. The portion of bulk defects is defined as the ratio of the final retained defects per unit area to the defects generated per unit area by the ion beam. The total number of defects per unit area generated by the ion beam in the range of $0-R_p$ is KR_p/v and the total number of final retained defects per unit area within the same range is CR_p; thus the portion of bulk defects is Cv/K and the portion of surface defects is $1-(Cv/K)$. Thus, the curves in Fig. 2 also define the portion of bulk defects as a function of αR_p.

To compare this model with experiment, we measured the strains of the films grown by IAMBE. A simple analysis of the strain modification was based on the assumption that the strains measured from the x-ray rocking curve analyses were proportional to the product of defect concentration and the defect-associated volume changes. Table I lists data associated with Ge films grown by the IAMBE processes. Figure 3 shows the dependence of the strains on the ion-to-atom flux ratio (J_i/J_a). The ion-to-atom flux ratio, J_i/J_a, is equal to
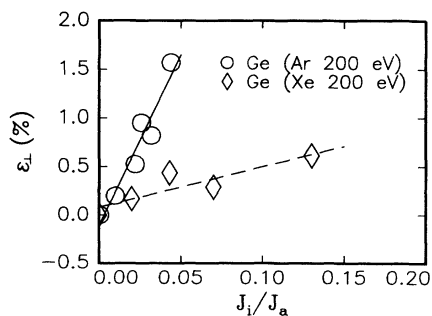

FIG. 3. The perpendicular strains of IAMBE Ge films with 200-eV Ar^+ bombardment and 200-eV Xe^+ bombardment at 300 °C, listed in Table I as a function of ion-to-atom ratio (J_i/J_a). The solid and dashed lines are fits for the moving boundary diffusion model in the growth-rate-limited regime.

K/v if one ion produces one defect. This is not necessary true for the case of defect incorporation. However, the ion-to-atom flux ratio is proportional to the value of K/v. Thus, for the case of defect incorporation, J_i/J_a which is directly measurable was used. We note that in these growth conditions the strains are roughly proportional to the ion-to-atom flux ratio only, and not the absolute ion flux. This suggests that the growth conditions are in the growth rate-limited regime since the final concentration in this regime is proportional to K/v. We can find the upper limit of the defect diffusivity, taking the growth rate as 0.1 nm/s, the defect production range estimated from the TRIM calculation is on the order of 1 nm for the above ion-energy condition, thus, $D \ll 10^{-15}$ cm^2/s for growth conditions to be in the growth-rate-limited regime. In previous experiments, we estimated an apparent activation energy for strain annihilation *obtained from the dependence of the strains on the growth temperatures* to be $Q=0.12$ eV.[7] If we use this activation energy and put it into the condition $D \ll 10^{-15}$ cm^2/s, we find that the pre-exponential factor, at 600 K, is $D_0 \ll 10^{-14}$ cm^2/s. This value implies a diffusion site density which is too low to be consistent with ordinary bulk thermal diffusion, and thus suggests the apparent activation energy obtained from the growth temperature dependence is *not* the true activation energy for a single rate-limited bulk defect diffusion process. The estimated activation energy may instead reflect the thermal spike energy deposited by the bombarding ions. Thus, we will consider the temperature rise in the subsurface region of a film due to the energy deposited by the energetic ions.

2. Cascade-assisted diffusion

An energetic particle striking a target will generate a cascade. Cascade recovery consists in principle of two parts, (i) athermal recovery and (ii) thermal recovery. The athermal recovery is due to the fact that there are both vacancies and interstitials inside the cascade region. The thermal recovery of the cascade is due to the local heating (thermal spike) which provides thermal energy to the defects. The fact that (i) the defects left after the events of cascade recovery are stable at the growth temperature and (ii) nonetheless we measured a very low apparent activation energy suggests that a possible explanation for the apparent activation energy in the growth temperature dependence of the strain annihilation is related to cascade-assisted defect diffusion. The final defects generated by the ion beam have an activation energy for movement much larger than the apparent activation energy.

The thermal spike concept has been used in sputtering and ion mixing. Several attempts at calculation of the temperature evolution inside a cascade region[18-20] have been made; we follow Vineyard's calculation of the temperature evolution inside a cylindrical thermal spike,[20] which has been successfully applied to explain the ion-beam mixing data.[21] It is important to remember the basic assumptions of the thermal spike model that the heat conduction equation is valid over the microscopic region and short time scale involved. The medium is con-

sidered to have a thermal conductivity κ, a heat capacity C_h, and a density ρ. The major contribution of the spike-induced jumps of the defects is from the core region at the beginning of the time; thus, for simplicity and to a first-order approximation, we assume that the heat capacity and the thermal conductivity are temperature independent at high temperature. Consider the liberation of the heat per unit length, F_d, at a point at the origin at time, $t=0$, with the initial medium temperature equal to the substrate growth temperature T_g; the temperature $T(s,t)$ at position s and time t corresponding to the solution for the heat conduction equation is

$$T(s,t)=\frac{F_d}{4\pi\kappa t}\exp\left[-\frac{\rho C_h s^2}{4\pi\kappa t}\right]+T_g \ . \tag{3}$$

The number of jumps per unit time contributed from the spike for a defect with a migration activation energy Q_m and an attempt frequency v is

$$\eta=J_i v\int_0^\infty 2\pi s\,ds\int_{t_0}^\infty\left\{\exp\left[-\frac{Q_m}{k_B T(r,t)}\right]\right.$$
$$\left.-\exp\left[-\frac{Q_m}{k_B T_g}\right]\right\}dt \ , \tag{4}$$

where J_i is the ion flux and k_B is the Boltzmann constant. The initial width of the cylindrical spike is determined by the starting time t_0. This cylindrical spike is assumed to have influence on the subsurface region only. We performed numerical integration of Eq. (4) with parameters $F_d=150$ eV/nm estimated from TRIM simulation of 200-eV Ar^+-bombarded Ge, $J_i=3\times10^{13}$ ions/cm^2 s, $C_{hp}=27$ J/mole K is the heat capacity for liquid Ge taken from Ref. 22, and $\kappa=0.014$ watt/cm K, as suggested by Thompson and Nelson.[23] The adjustable parameters are the activation energy for the defect migration and the starting time t_0, which corresponds to the initial distribution of the deposited energy[18] or the time needed to establish the Maxwell-Boltzmann distribution, i.e., local thermal equilibrium, which ranges between 10^{-12} and 10^{-13} s.[24] The effective diffusivity can be defined from Eq. (4) as $D=D_0[\eta/v+\exp(-Q_m/K_B T_g)]$, where D_0 is the preexponential for thermal diffusion.

Figure 4 shows three curves of effective diffusivity with (i) $Q_m=1.5$ eV and $t_0=4\times10^{-13}$ s, (ii) $Q_m=2$ eV and $t_0=4\times10^{-13}$ s, and (iii) $Q_m=2.5$ eV and $t_0=4\times10^{-13}$ s. The starting time $t_0=4\times10^{-13}$ s is in the range of the cascade duration[24] and consistent with the molecular-dynamic simulation.[25] The apparent activation in the first curve is $Q_a=0.08$ eV, in the second curve $Q_a=0.1$ eV, and in the third curve $Q_a=0.12$ eV. The experimental data points were the growth temperature dependence of strains of Ge films grown with 200-eV Ar^+ ion bombardment and ion-to-atom flux ratio, $J_i/J_a=0.02$. We can define a transition temperature, T_{tr}, above which the defect diffusion is thermally activated and below which the defect diffusion is cascade assisted. The transition
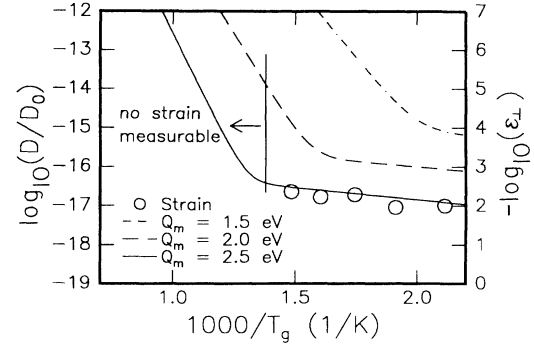

FIG. 4. Normalized diffusivity as a function of temperature for different activation energies of defect migration. All curves are calculated with $t_0=4\times10^{-13}$ s, $F_d=150$ eV/nm, and $J_i=3\times10^{13}$ ions/cm^2-s. The experimental data points were the growth temperature dependence of strains of Ge films grown with 200-eV Ar^+ ion bombardment and ion-to-atom flux ratio, $J_i/J_a=0.02$.

temperature is written as

$$T_{tr}=\frac{Q_m}{k_B}\left[\ln\left[\frac{v}{\eta}\right]\right]^{-1} \ . \tag{5}$$

As we can see from Fig. 4, the transition temperature for the third curve is about 800 K. In previous work, we find that no strain can be detected for 200-eV Ar^+-bombarded Ge films with an ion-to-atom flux ratio, $J_i/J_a=0.02$ at growth temperatures above 800 K,[7] and that the defects are mobile at 800 K upon post-growth annealing of the strained films.[8] Two points in Fig. 4 should be remarked: (i) the experimental data (strains) for value of $1000/T_g$ below 1.4 was not measurable by the x-ray rocking curve; and (ii) the experimental data points were intentionally shifted to lie on the third curve to show that the apparent activation energy obtained from the growth temperature dependence of the strains and the transition temperature are similar to the third curve. A fair agreement of both apparent activation energy and transition temperature between the experimental observation and the calculation was found to be $Q_m=2-2.5$ eV and $t_0=4\times10^{-13}$ s. The corresponding pre-exponential factor is 2.32×10^{-16} cm^2/s, which also agrees with the condition for the growth-rate limited regime. Note that the choice of t_0 and Q_m is not unique. As t_0 decreases the apparent activation energy and T_{tr} decreases, and when Q_m increases the apparent activation energy and T_{tr} increase. Although the results of the calculation of the spike evolution is not exact due to the assumptions made and owing to the nonunique choice of t_0 and Q_m, the agreement between the experimental observation and this simple calculation suggests that the energy deposited by the energetic particle plays an important role in the defect diffusion process. Equation (4) has also been numerically integrated for finite T_g by Gilmore, Haeri, and Sprague[26] to investigate the contribution of the thermal spike effect on the adatom surface diffusivity during ion-beam-assisted deposition of Au on NaCl using 100-eV

Ar$^+$ ions. They concluded that the thermal spike would produce a negligible effect on adatom diffusivity for typical adatom densities. In contrast to the calculation of Gilmore, Haeri, and Sprague, we find that the thermal spike has a profound effect on the apparent activation energy of defect diffusion in spite of the small effective diffusivity.

Meyer et al.[27] have also obtained low activation energies, 0.15 eV for 800-nm $Si_{0.4}Ge_{0.6}$ film and 0.5 eV for 300-nm $Si_{0.7}Ge_{0.3}$ film grown on Si(100) by ion-beam sputtering deposition, from the growth temperature dependence of film stresses. Since the film thicknesses are above the critical thicknesses for dislocation formation, the films are expected to be at least partially relaxed. The low activation energy observed by Meyer et al. suggests that the major driving force for strain relaxation is the defect diffusion and the cascade-assisted diffusion is the dominant mechanism for defect migration.

We note also that Windischmann has provided a detail analysis of the ion peening model to explain the intrinsic stresses of thin films prepared by the ion-beam sputtering.[28] The ion peening model, which is based on the knock-on linear cascade theory of transition sputtering proposed by Sigmund,[29] can explain the intrinsic stresses for a variety of films deposited at a temperature where the defect mobility is sufficiently low that the growth conditions can be classified to be in the growth-rate limited regime and can provide a basis for the description of the total defect flux K. The combination of the ion peening model and the moving boundary diffusion model is straightforward and should be able to be used to analyze a variety of materials deposited with energetic ion beams involved.

B. Ion incorporation

The continuous moving boundary diffusion problem used in this analysis of defect-related strain produces parametric dependencies that are qualitatively similar to the discrete multisite model presented by Ni et al.[14] Hence it seems reasonable to compare this analysis with the discrete model, which can be done by setting $K = \gamma J_i$ for dopant incorporation, where γ is the incorporation coefficient which is the fraction of the ions which rest on or inside the target. The incorporation coefficient for fixed ion species and substrate is a function of ion energy and substrate temperature. In the case of Sb ion incorporation into Si, the incorporation probability is assumed to be unity for all ion energies and for all substrate temperatures, i.e., $K = J_i$. We can also generalize the moving boundary diffusion model by additional terms in Eq. (1) which act to model dopant segregation. In the temperature regime used in the experiments of Ni et al.[14] the diffusivity of the dopant at 900°C for Sb atoms in Si is comparable to vR_p, thus the dopant incorporation probability $(Cv/J_i$, the same as the definition of the bulk defects) will rise quickly at low growth rate and saturate. Figure 5 shows the data of incorporation probability of Sb atoms as a function of Si growth rate taken from Ref. 14 and the calculated curves using the moving boundary diffusion model. We find that the calculated curves can-
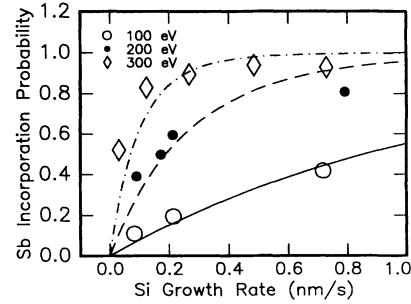

FIG. 5. Sb ions incorporation probability as a function of ion energy and the Si growth rate. The experimental data are taken from Ref. 14. The curves are calculated from Eq. (2ii) with fixed $R_p/\sqrt{2}\Delta R_p = 2.357$ used in Ref. 14. The parameter for the solid line is $R_p/D = 0.8$ s/nm, for the dashed line $R_p/D = 3.7$ s/nm, and for the dotted line $R_p/D = 10$ s/nm.

not fit the experimental data with a single activation energy. We follow the description in Ref. 14 to choose the Sb projected ranges for different energies, $R_p = 0.25$ nm for 100-eV ions, $R_p = 0.53$ nm for 200-eV ions, and $R_p = 0.81$ nm for 300-eV ions, and fix $\Delta R_p/R_p = 0.3$. The activation energies at 900°C obtained from 100-eV Sb ion-beam data is $D = 3.0 \times 10^{-15}$ cm^2/s, from 200-eV Sb ion-beam data $D = 1.4 \times 10^{-16}$ cm^2/s, and from 300-eV Sb ion-beam data $D = 8.1 \times 10^{-16}$ cm^2/s. Note that the diffusivities approach the bulk value as ion energies increase. The diffusivity values obtained lie in the range of those assumed for the third and fourth layers in Ni's model. The phenomenon of lower activation energy in the subsurface region suggests that the multisite model is necessary for dopant incorporation using low-energy ion beams.

The temperature dependence of the dopant incorporation has two cases: (i) the transition temperature between thermal diffusion and cascade-assisted diffusion is in the growth-rate-limited regime; and (ii) the transition temperature is in the diffusion-limited regime. From Eqs. (4) and (5), the number of jumps per unit time contributed from the spike for a defect is proportional to the ion flux J_i; thus, the transition temperature increases as the ion flux increases. For all other growth parameters fixed except the ion flux, case (i) corresponds to a low incoming ion flux and case (ii) corresponds to a high incoming ion flux. In case (i), the effective diffusivity dominated by the cascade-assisted diffusion at low temperature is so small such that $\alpha R_p \gg 1$. This indicated that the temperature dependence of the dopant incorporation would not be perturbed by the cascade-assisted diffusion, since the dopant incorporation process was already in the growth-rate-limited regime. In case (ii), the cascade-assisted diffusion will dominate the diffusion process before the dopant incorporation process can be classified to be in the growth-rate-limited regime. This indicates that the effective diffusivity dominated by the cascade-assisted diffusion is so large such that αR_p is comparable to unity or much smaller than unity. Thus the approach of the dopant incorporation probability to unity is no longer controlled by the thermal activation energy; instead, is
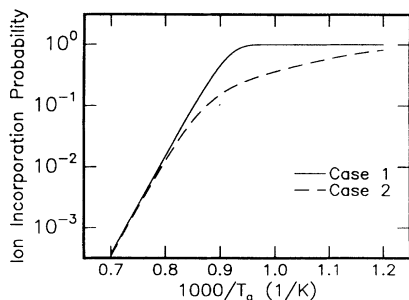
FIG. 6. The defect incorporation probability as a function growth temperature. In case 1 (solid line), the thermal diffusivity dominates from $\alpha R_p = 0$ to $\alpha R_p \gg 1$. In case 2 (dashed line), the cascade-assisted diffusivity extends down to $\alpha R_p < 1$. The parameters used to calculate these two curves are $D_0 = 0.214$ cm²/s and $Q_m = 3.2$ eV for thermal diffusivity, $D_0 = 1 \times 10^{-16}$ cm²/s and $Q_a = 0.6$ eV for cascade-assisted diffusivity in case 1, and $D_0 = 1 \times 10^{-13}$ cm²/s and $Q_a = 0.6$ eV for cascade-assisted diffusivity in case 2.

controlled by the apparent activation energy due to cascade-assisted diffusion below the transition temperature. The curve 1 in Fig. 6 shows case (i), in which the effect of cascade-assisted diffusion does not play an important role in dopant incorporation, and curve 2 corresponds to case (ii), in which a second activation energy which reflects the effective diffusivity due to cascade-assisted diffusion plays a role in the ion incorporation probability. The parameters used in calculating these two curves are shown in the figure caption. The only difference is a change in the effective pre-exponential factor for cascade-assisted diffusion which can be adjusted by changing the ion flux. The experimental conditions in Ref. 14 correspond to case (i) in Fig. 6 due to the low ion flux ($J_{Sb} = 4 \times 10^7 - 4 \times 10^{10}$ ions/cm²-s) and high growth temperature ($T_g > 600$ °C) which were used. Figure 7 shows the data points taken from Ref. 14 and the curves calculated using Eq. (2ii) with $v = 0.17$ nm/s, $R_p = 1.1$
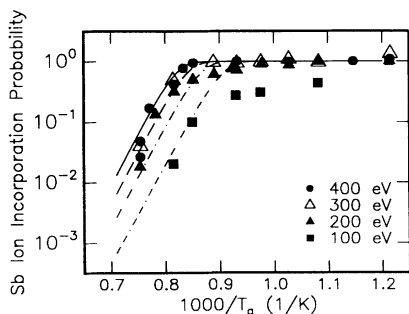

FIG. 7. The temperature dependence of the dopant incorporation for different Sb ion energies. The data points are taken from Ref. 14. All lines are calculated with $D_0 = 0.214$ cm²/s and $v = 0.17$ nm/s. The values of R_p, 0.25, 0.53, 0.81, and 1.1 nm, and the values of activation energy for Sb ions in Si, 3.23 eV (dot-dashed-dashed line), 3.31 eV (dot-dashed line), 3.36 eV (dashed line), and 3.40 eV (solid line), correspond to 100, 200, 300, and 400 eV Sb ions, respectively.

nm for 400-eV Sb ions, and the choices of R_p at other different energies are the same as before. $D_0 = 0.214$ cm²/s for all energies, the activation energy is 3.23 eV for 100-eV Sb ions, 3.31 eV for 200-eV Sb ions, 3.36 eV for 300-eV Sb ions, and 3.40 eV for 400-eV Sb ions. The activation energies for thermal diffusion are chosen this way so that the previous diffusivities at 900 °C for different ion energies, obtained from the growth-rate-dependence of dopant incorporation are numerically equal in the context of the present single activation energy model. The calculated curves fit the data points well for ion energies larger than 300 eV while giving poor fits for lower energy ion beams. It is also interesting to compare the difference between the dopant and inert gas incorporation. Our previous measurements of the Xe concentration trapped inside Ge films[7] indicated that the incorporation probability of Xe was only about 3% even when the growth conditions were in the growth-rate-limited regime. This suggests the importance of the incorporation coefficient.

The major deviation of the moving boundary diffusion model from low-energy ion incorporation data is due to the multiple activation processes for dopant incorporation such as adsorption and desorption of the ions at the surface, the difference between surface phonon and bulk phonon, the electronic state near surface, and the thermal spike effect which all could contribute to the multiple activation processes. All the curves in Figs. 6 and 7 are calculated from Eq. (2ii), which is a solution subjected to the boundary condition that $N(0) = 0$, which is not a proper condition for low-energy dopant incorporation processes and predicts that no dopant incorporation will occur through adsorption and desorption processes. Since the simple moving boundary diffusion model neglects the depth dependence of the diffusivity of the defects, the quantitative use of this simple model is only suitable for higher energy ion beams (e.g., $E_i > 300$ eV for Sb ions incorporation into Si).

IV. CONCLUSIONS

The IAMBE processes can be modeled using a continuous moving boundary diffusion model. The defect concentrations generated by the ion beam are proportional to the ion-to-atom flux ratio in the growth-rate-limited regime. The definitions of surface defects (defects that will come out to the surface) and bulk defects (defects that will be trapped inside the bulk) were defined in a dynamic term as a function of the growth rate, defect production range, and defect diffusivity. The low apparent activation energy obtained from the growth temperature dependence of the strain annihilation is explained by cascade-assisted defect diffusion. In IAMBE processes, the ion beam generates a cascade which undergoes athermal and thermal recovery. The defects left after cascade recovery have a diffusivity determined by the relative importance of the thermal diffusion and subsequent cascade-assisted diffusion. The same equation can also be used to describe the dopant incorporation processes and reasonable agreement with experimental data can be found for higher ion energies. In low-energy ion incorporation processes, the

defect incorporation may accompany the dopant incorporation. In general, the activation energies for defect diffusion and dopant diffusion are not the same. Neglecting the interaction between defects and dopants, one could define transition temperatures for both defects and dopants. For enhancing dopant incorporation while minimizing defect incorporation, one should also avoid the dopant incorporation processes at the temperature regime below T_{tr}, where the defects generated by the ion beam are stable. The moving boundary diffusion model gives a unified view of dopant and defect incorporation processes. The multiple activation site in the surface region can be done by adding layers in the surface region with different diffusivities and continuous boundary conditions at each interface. However, the model can only be used to describe the incorporation of pointlike defects. When extended defects formation or the segregation of the dopants are involved, the simple model needs to be modified.

*Present address: Gordon McKay Laboratory of Applied Science, Harvard University, Cambridge, MA 02138.

[1]J. E. Greene, CRC Crit. Rev. Solid State Mater. Sci. 2, 47 (1983).

[2]J. Y. Tsao, E. Chason, K. M. Horn, D. K. Brice, and S. T. Picraux, Nucl. Instrum. Methods B 39, 72 (1989).

[3]E. Chason, J. Y. Tsao, K. M. Horn, and S. T. Picraux, J. Vac. Sci. Technol. B 7, 332 (1989).

[4]E. Chason, J. Y. Tsao, K. M. Horn, S. T. Picraux, and H. A. Atwater, J. Vac. Sci. Technol. A 8, 2507 (1990).

[5]K. M. Horn, J. Y. Tsao, E. Chason, D. K. Brice, and S. T. Picraux, J. Appl. Phys. 69, 243 (1991).

[6]C.-H. Choi, L. Hultman, and S. A. Barnett, J. Vac. Sci. Technol. A 3, 1587 (1990).

[7]C. J. Tsai, H. A. Atwater, and T. Vreeland, Appl. Phys. Lett. 57, 2305 (1990).

[8]C. J. Tsai, P. Rozenak, H. A. Atwater, and T. Vreeland, J. Cryst. Growth 111, 931 (1991).

[9]P. C. Zalm and L. J. Beckers, Appl. Phys. Lett. 41, 167 (1982).

[10]T. Itoh, T. Nakamuru, M. Muromachi, and T. Sugiyama, Jpn. J. Appl. Phys. 16, 553 (1977).

[11]C. Schwebel, F. Meyer, G. Gautherin, and C. Pellet, J. Vac. Sci. Technol. B 4, 1153 (1986).

[12]F. Meyer, C. Schwebel, C. Pellet, G. Gautherin, A. Buxbaum, M. Eizenberg, and A. Raizman, Thin Solid Films 184, 117 (1990).

[13]T. Ohmi, K. Hashimoto, M. Morita, and T. Shibata, J. Appl. Phys. 69, 2062 (1991).

[14]W.-X. Ni, J. Knall, M. A. Hasan, G. V. Hansson, J.-E. Sundgren, S. A. Barnett, L. C. Markert, and J. E. Greene, Phys. Rev. B 40, 10 449 (1989).

[15]W. J. Bartels, J. Vac. Sci. Technol. B 1, 338 (1983).

[16]C. R. Wie, T. A. Tombrello, and T. Vreeland, J. Appl. Phys. 59, 3743 (1986).

[17]A. K. Myers-Beaghton and D. D. Vvedensky, Phys. Rev. B 42, 5544 (1990).

[18]R. Kelly, Radiat. Eff. 32, 91 (1977).

[19]P. Sigmund and C. Claussen, J. Appl. Phys. 52, 990 (1981).

[20]G. J. Dienes and G. H. Vineyard, Radiation Effects in Solids (Interscience, New York, 1957); G. H. Vineyard, Radiat. Eff. 29, 245 (1976).

[21]Y. T. Cheng, Mater. Sci. Rep. 5, 47 (1990).

[22]I. Barin, Thermochemical Data of Pure Substances (VCH, New York, 1989), Pt. 1.

[23]M. W. Thompson and R. S. Nelson, Philos. Mag. 7, 2015 (1962).

[24]M. W. Thompson, Defects and Radiation Damage in Metals (Cambridge University Press, London, 1969).

[25]R. S. Averback, Nucl. Instrum. Methods B 15, 675 (1986).

[26]C. M. Gilmore, A. Haeri, and J. A. Sprague, Thin Solid Films 165, 359, 1988.

[27]F. Meyer, M. Zafrany, M. Eizenberg, R. Beserman, C. Schwebel, and C. Pellet, J. Appl. Phys. 70, 4268 (1991).

[28]H. Windischmann, J. Appl. Phys. 62, 1800 (1987).

[29]P. Sigmund, in Sputtering by Particle Bombardment I, edited by R. Behrisch (Springer, Berlin, 1981), Chap. 2.